# Dynamic Image Sampling Using a Novel Variance Based Probability Mass Function

Simon Grosche, Michael Koller, Jürgen Seiler, *Senior Member, IEEE*, and André Kaup, *Fellow, IEEE*

***Abstract*—Incremental sampling can be applied in scientific imaging techniques whenever the measurements are taken incrementally, i.e., one pixel position is measured at a time. It can be used to reduce the measurement time as well as the dose impinging onto a specimen. For incremental sampling, the choice of the sampling pattern plays a major role in order to achieve a high reconstruction quality. Besides using static incremental sampling patterns, it is also possible to dynamically adapt the sampling pattern based on the already measured data. This is called dynamic sampling and allows for a higher reconstruction quality, as the inhomogeneity of the sampled image content can be taken into account. Several approaches for dynamic sampling have been published in the literature. However, they share the common drawback that homogeneous regions are sampled too late. This reduces the reconstruction quality as fine details can be missed. We overcome this drawback using a novel probabilistic approach to dynamic image sampling (PADIS). It is based on a data driven probability mass function which uses a local variance map. In our experiments, we evaluate the reconstruction quality for scanning electron microscopy images as well as for natural image content. For scanning electron microscopy images with a sampling density of 35% and frequency selective reconstruction, our approach achieves a PSNR gain of +0.92 dB compared to other dynamic sampling approaches and +1.42 dB compared to the best static patterns. For natural images, even higher gains are achieved. Experiments with additional measurement noise show that for our method the sampling patterns are more stable. Moreover, the runtime is faster than for the other methods.**

***Index Terms*—Dynamic sampling, non-regular sampling, image reconstruction.**

## I. Introduction

MANY scientific imaging techniques in physics, biology and material science rely on a point-wise incremental acquisition of image data. Examples include scanning electron microscopy (SEM) [1], atomic force microscopy [2], [3], and Raman imaging [4]. For such applications, incremental sampling can greatly reduce the number of measurements by performing only a subset of all measurements [5], [6]. Fig. 1(a) shows a static incremental sampling process with a random sampling pattern. New sampling positions are incrementally added. At each step, a full resolution image can be reconstructed from the measured data. Since only a subset of all pixels is actually sampled, sparse sampling leads to a faster acquisition and less dose applied to the specimen. This is especially important in case of organic specimens but can even play a role for inorganic specimens. In both cases the sample may otherwise be damaged during the measurement [7].

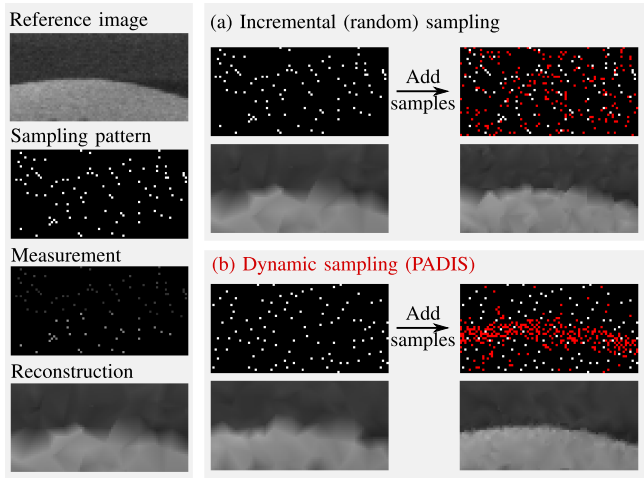


Fig. 1. Illustration of (a) static incremental sampling and (b) dynamic sampling. For dynamic sampling, the new sampling positions (red) are adapted to the already sampled content. Consequently, the reconstruction quality may increase.

In order to allow for a high reconstruction quality, the choice of the sampling positions plays a crucial role. In a first, simplistic attempt, one could reduce the number of samples by skipping several rows. Such a lineskip approach was further developed in [6], where wiggling lines were used instead of straight lines. In general, non-regular sampling patterns should be favored over regular sampling patterns since the latter introduce severe aliasing artifacts. Instead, non-regular sampling allows for the reconstruction of higher frequencies [8]–[10]. Besides random sampling strategies [1], [11], optimized sampling strategies which sample the image content more uniformly were developed [12].

Instead of using a fixed sampling pattern, the sampling pattern can be adapted to the content. Dahmen *et al.* [13] suggest to perform an initial fast scan of the entire image with decreased integration times, i.e., low signal to noise ratio. Then, the image is analyzed and important regions are scanned with a higher signal to noise ratio. In such a scenario, however, the data from the initial scan is either disregarded or has to be merged

Manuscript received June 10, 2020; revised September 1, 2020 and October 1, 2020; accepted October 4, 2020. Date of publication October 14, 2020; date of current version October 28, 2020. The associate editor coordinating the review of this manuscript and approving it for publication was Dr. Singanallur Venkatakrishnan. *(Corresponding author: Simon Grosche.)*

The authors are with the Chair of Multimedia Communications and Signal Processing, Friedrich-Alexander University Erlangen-Nürnberg, 91058 Erlangen, Germany (e-mail: simon.grosche@fau.de; michael.koller@fau.de; juergen.seiler@fau.de; andre.kaup@fau.de).

Digital Object Identifier 10.1109/TCI.2020.3031077

with the second scan, which is not easily possible. Similarly, in [14] the entire image needs to be known before optimized sampling positions are derived. Another approach to adapt the sampling pattern to the content is to use dynamic sampling. For dynamic sampling, the new sampling positions depend on the already measured data and may therefore dynamically adapt to the image content as can be seen in Fig. 1(b). As initialization, a fixed, sparse pattern of low sampling density is used. Dynamic sampling is incremental but not static because the sampling pattern is not known in advance. As for the example in Fig. 1(b), dynamic sampling means that the new positions colored in red are adapted to the content of the image at the already sampled positions colored in white.

Intuitively, dynamic sampling may increase the reconstruction quality because regions with fine details could be sampled denser, whereas less detailed regions may be sampled less dense. Over the years, several authors proposed algorithms for dynamic image sampling. Merryman *et al.* [15] follow an approach for fluorescence microscopy, where high intensity values serve as indication for a region of interest that should be sampled denser. A more general approach is introduced by Dahmen *et al.* [16] suggesting the usage of a gradient based criterion for the placement of new pixels. Here, the gradients are calculated on the edges of the Delaunay triangulation of the already measured pixels. In a sophisticated approach, Godaliyadda *et al.* [17], [18] propose a supervised learning method (SLADS) which aims at learning a regression function that estimates the expected reduction of distortion for any possible new sampling position. A newer variant called SLADS-Net [19] adds a neural network to learn the regression function more precisely. In those works, a very good performance is observed for boundaries between mostly homogeneous objects. Such boundaries are of special interest for segmentation tasks, for example. Both approaches perform very well in finding boundaries that can be identified from the previous measurements. However, this leads to sampling patterns where presumably homogeneous regions are sampled at a very low sampling density. Consequently, important details in presumably homogeneous regions may not be detected and the texture of the objects is not expected to be sampled optimally.

To overcome this problem, in this paper, we propose a modified objective when choosing the sampling positions. Instead of mainly performing well on the reconstruction of the boundaries between mostly homogeneous objects, we aim at properly reconstructing the entire image including its textures and small details. In addition to a broad range of grayscale SEM images, our dynamic sampling approach shall additionally be tested for the acquisition of natural images where diverse textures and structures can be present. Other than for SEM images, a hardware implementation for dynamic sampling of natural images is not expected to be possible. However, the dynamic sampling of natural images is also considered to be relevant since it may be used for future image compression techniques. Existing works on image compression with adaptive sampling such as [20] use content adaptive sampling patterns that are not dynamic, i.e., the information on the sampling positions needs to be coded, too. In contrast to that, the sampling pattern in [21] is fixed and does not need to be coded. For future compression frameworks based on dynamic sampling, the advantages from both approaches could be combined. The sampling positions could be dynamically adapted to the content but at the same time no information about the positions of the samples has to be transmitted to the receiver. This is the case since the new sampling positions can be calculated from all previous positions and the already transmitted values. The initial pattern can be hard-coded as is independent of the content. Besides this, we aim at developing a dynamic sampling strategy that can be accomplished without the need to retrain the algorithm for specific datasets. This is different from the main objective of SLADS and SLADS-Net where the training images are intended to be very similar to the testing images such that overfitting problems could easily occur.

To accomplish these objectives and to overcome the aforementioned disadvantages of the methods from literature, we propose a *probabilistic approach to dynamic image sampling* (PADIS). It is based on the static incremental sampling technique presented in [12] and extends the probability mass function defined in [12] such that information about the already measured data is considered.

This paper is organized as follows: In Section II, we review the concepts of static incremental sampling and dynamic sampling. In Section III, we review three state-of-the-art literature algorithms for dynamic image sampling. Afterwards, we describe the novel PADIS in Section IV. In Section V, we compare PADIS to the other approaches. Reconstruction results are evaluated in terms of PSNR using three different reconstruction algorithms and two different image datasets. Moreover, visual examples are provided, an experiment with measurement noise is performed and the required runtimes for the generation of the different dynamic sampling patterns are compared.

## II. Definition of Static and Dynamic Sampling

In this section, we briefly explain the notion of static incremental sampling and dynamic sampling. The sub-sampled image $\tilde{f}[x,y]$ can be described as the multiplication of the reference image $f[x,y] \in [0,1]$ of size $X \times Y$ pixels with a binary pattern $b[x,y] \in \{0,1\}$, i.e.,

$$\tilde{f}[x,y] = f[x,y] \cdot b[x,y] \quad \forall x,y. \tag{1}$$

In incremental sampling, more measurements are added in each step. The binary patterns $b^i[x,y]$ include all pixels that are measured up to the $i$-th step. The samples added in the $(i+1)$-th step can then be calculated as

$$\delta_b^{i+1}[x,y] = b^{i+1}[x,y] - b^i[x,y]. \tag{2}$$

Per definition, *incremental* means that all pixels measured in previous steps are also available in the current step, i.e.,

$$\{(x,y)|b^i[x,y]=1\} \subset \{(x,y)|b^{i+1}[x,y]=1\}, \tag{3}$$

and all new samples were not available before, i.e.,

$$\{(x,y)|\delta^{i+1}[x,y]=1\} \cap \{(x,y)|b^i[x,y]=1\} = \emptyset. \tag{4}$$

The sampling equation in the $i$-th step then reads

$$\tilde{f}^i[x,y] = f[x,y] \cdot b^i[x,y] \quad \forall x,y. \tag{5}$$

Both static incremental sampling and dynamic sampling are incremental in the just defined sense. In case of a static sampling, all patterns $b^{i+1}[x, y]$ are independent of the already sampled data, i.e. they only depend on the previous sampling pattern ensuring that they are incremental,

$$b^{i+1}[x, y] = g^{\mathrm{stat}}(b^i[x, y]). \tag{6}$$

Different algorithms may be used to design the functional dependence $g^{\mathrm{stat}}(b^i[x, y])$, e.g., distributing the new samples randomly or using an optimized strategy as in [12]. For dynamic sampling, the function $g^{\mathrm{dyn}}$ additionally depends on the already measured data from the previous step,

$$b^{i+1}[x, y] = g^{\mathrm{dyn}}(b^i[x, y], \tilde{f}^i[x, y]). \tag{7}$$

This dependence allows an adaptation of the sampling pattern to the already sampled data.

For both sampling types, a reconstruction of the full image can be performed in the $i$-th step yielding an approximation $\hat{f}^i[x, y]$. Since all patterns in this paper are incremental, we drop the usage of this word for convenience.

Equation (7) assumes that the measurements are immediately available. This assumption is idealistic but commonly done in literature [17], [18], [20], [22]. In a hardware implementation, depending on the actual scenario, this may not be the case and some of the measurements might be delayed. We are confident that such implementation details could be incorporated in the proposed algorithm, if needed. We would like to note that in case of image compression based on dynamic sampling, the used assumption is perfectly valid.

## III. Dynamic Image Sampling in Literature

In the following, the state of the art approaches used as reference are discussed. Additionally, we identify the disadvantages they have in common.

### A. Gradient Based Approach

In case of the gradient based approach in [16], new sampling positions are added based on a gradient criterion. The algorithm is initialized with a static sampling pattern. Then, new sampling positions are added as described in the previous section. For a given sampling pattern $b^i[x, y]$, the gradients between neighboring measurements are calculated. To identify the neighborhood relations, the Delaunay triangulation is used. The new sampling positions are placed inside those Delaunay triangles where the gradients along the edges are maximal. All gradients are recalculated after the sampling density has increased by a fraction $N_+$. A reference algorithm was kindly provided by the authors.

### B. SLADS and SLADS-NET

A more sophisticated approach is the supervised learning approach for dynamic sampling (SLADS) proposed in [17], [18]. An implementation is available from the authors. In SLADS, a non-linear regression function estimating the reduction of distortion from several features is trained using a training dataset and a least squares regression. The reduction of distortion is defined as the change of the mean absolute error of the reconstructed image, when a new sampling position is added to the sampling pattern. The newly added sampling position is then chosen such that the estimated reduction in distortion is maximal. In a variation of the algorithm, several samples are added in each step to reduce the computational cost. In addition to a training needed to compute the parameters of the feature extraction, a second hyper-parameter called $c$ is required to be learned using the training data.

SLADS is an improvement of a previous work from the same group. In their model-based dynamic image sampling (MBDS) [22], the new sampling positions are placed such that the expected posterior variance is maximized. MBDS is based on a Monte Carlo approach to estimate the posterior variance at every unmeasured position. It is claimed to be much slower than SLADS [17]. Additionally, SLADS shows superior reconstruction quality according to the authors. In our experiments, we therefore use SLADS for which, other than for MBDS, an implementation is available.

SLADS-Net [19] is the most recent development of SLADS. It builds upon SLADS but learns the regression function using a neural network based approach. It is argued to be faster than SLADS and shows better performance than SLADS [19]. It is also shown that SLADSNet performs better in case the training and testing data are less similar [19]. When we compare with SLADSNet, we use a pre-trained model for continuous data provided by the authors.

### C. Common Disadvantages

The gradient based approach [16], MBDS [22], SLADS [17], [18], as well as SLADS-Net [19] perform very well in dynamically sampling the boundaries between mostly homogeneous objects. However, the approaches strongly focus on already identified structures, and other regions are sampled at a very low density. Consequently, presumably homogeneous regions cannot be recovered in case fine details or texture-like structures are present. All structured regions that are not identified by the initial sampling pattern are subsequently hindered to be sampled. Instead, new samples are placed close to already found details such that these are sampled better. This can be explained by the maximization criteria utilized by those algorithms as detailed in the previous sub-sections. However, for general purpose applications, fine details as well as texture are important. We see this as a limitation of the existing approaches that shall be overcome in this work.

## IV. Probabilistic Approach to Dynamic Image Sampling (PADIS)

In this section, we propose PADIS,[1] a new algorithm for dynamic image sampling. Using PADIS, we aim at overcoming the disadvantage of the state-of-the-art methods described in Section III-C. PADIS extends the static sampling approach presented in [12]. Other than the probability mass function

[1]The source code of PADIS is provided [Online]. Available: https://gitlab.lms.tf.fau.de/LMS/PADIS

in [12], our new probability mass function adapts to the values of the already measured data. Compared to the gradient based approach [16], MBDS [22], SLADS [17], [18], and SLADS-Net [19], we do not position the new samples based on a maximization criterion. Instead, we draw the sampling positions from the data driven probability mass function.

### A. Initial Sampling Pattern

As all other dynamic sampling approaches, PADIS starts with an initial sampling pattern $b^0[x,y]$ with a low sampling density $d_{\text{init}} \ll 100\%$. The initial sampling density should be low enough to achieve a good content adaptation but high enough to initially cover most parts of the image in order not to miss out important details. With an initial sampling pattern at hand, our aim is to find a new sampling pattern $b^{i+1}$ as a function of the previous sampling pattern $b^i$ and the already sampled values $\tilde{f}^i$.

### B. Estimation of the Local Variance

The first step to decide which sampling positions to choose in the $(i+1)$-th step is to estimate the local variance of the image for every pixel position. It is used to identify heterogeneous regions of the image that will be sampled with a higher sampling density than homogeneous regions. This is expected to result in a better performance of the reconstruction. The estimated variance at the position $(x,y)$ only depends on the $(2s_b+1)\times(2s_b+1)$ block of the non-regularly sampled image $\tilde{f}^i[x,y]$ around the current position and is defined as

$$v[x,y] = \sum_{m=-s_b}^{s_b}\sum_{n=-s_b}^{s_b} \frac{w[m,n](\tilde{f}^i[x+m,y+n]-\mu)^2}{N}, \tag{8}$$

with $\mu$ being the mean of the sampled pixel values of the current image block,

$$\mu = \frac{\sum_{m,n=-s_b}^{s_b} \tilde{f}^i[x+m,y+n]}{\sum_{m,n=-s_b}^{s_b} b^i[x+m,y+n]}, \tag{9}$$

and $N$ being a normalization constant,

$$N = \max_{\tilde{m},\tilde{n}}(w[\tilde{m},\tilde{n}]) \cdot \sum_{m,n=-s_b}^{s_b} b^i[x+m,y+n], \tag{10}$$

accounting for different sampling distributions and densities. $w[m,n]$ is an exponential weighting function

$$w[m,n] = b^i[m,n]\exp\left(-\frac{m^2+n^2}{s_b^2}\right). \tag{11}$$

The summations in (9) and (10) could in principle be zero. However, this is prevented by choosing a large enough block size $s_b$ as well as a large enough initial sampling density $d_{\text{init}}$.

The values of the variance map are normalized resulting in the normalized variance map $v'[x,y] \in [0,1]$,

$$v'[x,y] = \frac{v[x,y]}{\max_{\tilde{x},\tilde{y}}(v[\tilde{x},\tilde{y}])}. \tag{12}$$

An example is shown in Fig. 2(c).

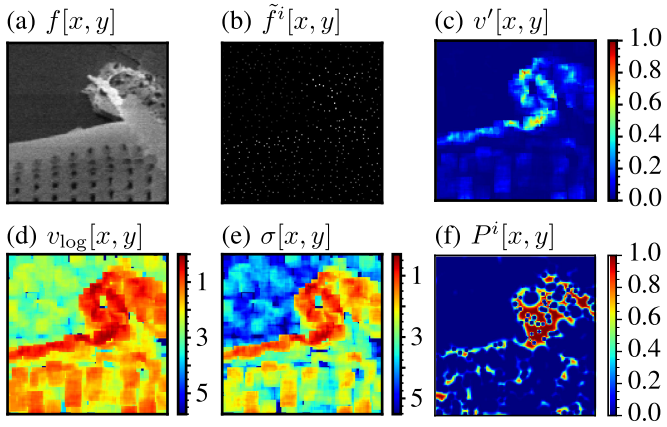


Fig. 2. Example for the auxiliary functions needed in PADIS. (a) Reference image $f[x,y]$ of size $128\times128$ pixels cut out of an SEM image. (b) Sampled image $\tilde{f}^i[x,y]$ at a sampling density of 3%. (c) Normalized variance map $v'[x,y]$ and (d) corresponding logarithmic variance map $v_{\log}[x,y]$. (e) Function $\sigma[x,y]$ which is used as local standard deviation in the probability mass function $P[x,y]$ shown in (f).

### C. Probability Mass Function

The just derived normalized variance map $v'[x,y]$ is now used to derive the probability mass function for choosing the next sampling positions.

In principle, it would be possible to use the variance map as probability mass function or even directly sample at the maximal value of the variance map, which would then be closely related to MBDS [22]. Such approaches are regarded to be undesirable because one would mostly create new sampling positions right next to already sampled pixels. This is, however, non-optimal, because the sampling then focuses strongly on the heterogeneous parts and the same problem as explained in Section III-C for the reference algorithms arises. Here, we use the variance map to extend the probability density based approach which was used in [12] to create optimized static sampling patterns. It ensures that pixels next to already sampled pixels are chosen with very low probability while at the same time regions with a high variance are preferred without completely ignoring homogeneous regions. Other than in [12], the probability mass function in PADIS is adapted depending on the measured values to achieve a dynamic sampling.

As a first step, we define the logarithmic variance map

$$v_{\log}[x,y] = -\log_{10} v'[x,y]. \tag{13}$$

Applying the logarithm reveals the less dominant structures of the image. In Fig. 2(d) the impact of the logarithm is clearly visible as much more structure of the image becomes visible compared to the normalized variance map.

To get an impression of the value range in the logarithmic variance map, the cumulative distribution function of $v_{\log}[x,y]$ is shown in Fig. 3 for the case of Fig. 2(d). It is clearly visible that most of the values are within a range between zero and approximately 3.7 for the given example.

In order to account for different image content, the logarithmic variance map is renormalized. While doing so, all values in $v_{\log}[x,y]$ above a certain threshold $l_{\max}$ are cut off. The value

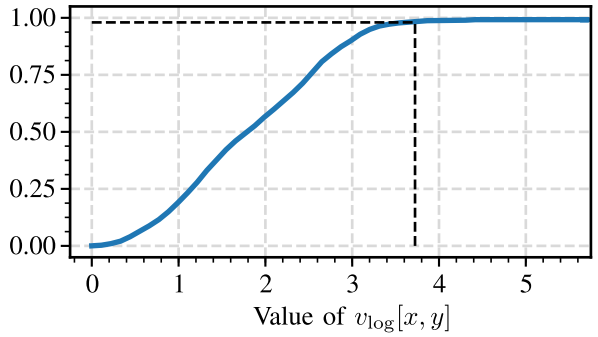


Fig. 3. Cumulative distribution function of $v_{\log}[x, y]$. Most of the values of $v_{\log}[x, y]$ are below 3.7.

of the threshold $l_{\max}$ is set such that the cumulative distribution function reaches a limit of 98%. This yields a threshold of $l_{\max} \approx 3.72$ for the given example and is indicated with a dashed black line in Fig. 3.

We define the truncated and renormalized logarithmic variance map as

$$\sigma[x, y] = \begin{cases} \sigma_{\max} & v_{\log}[x, y] \geq l_{\max} \\ \sigma_{\max} \frac{v_{\log}[x,y]}{l_{\max}} & v_{\log}[x, y] < l_{\max} \end{cases}, \tag{14}$$

where the values are rescaled to the range $0 \ldots \sigma_{\max}$.

The selection of $\sigma_{\max}$ is an essential part of the adaptive sampling procedure. It is supposed to be a measure of the width around each pixel where new samples should be placed with low probability. We imply $\sigma_{\max}^2 \cdot d_{\mathrm{s}} = \text{const.}$ such that the total area covered by those regions of low probability is independent of the sampling density $d_s$. Therefore,

$$\sigma_{\max} = \gamma / \sqrt{d_{\mathrm{s}}}, \tag{15}$$

with a proportionality constant $\gamma$ which needs to be found in a parameter training. An example for the function $\sigma[x, y]$ is shown in Fig. 2(e).

In order to achieve the desired sampling, the truncated and renormalized logarithmic variance map $\sigma[x, y]$ is used as the local standard deviation of a Gaussian-like probability mass function from which the new sampling positions are drawn. The objective for this task is to assign high probabilities to heterogeneous areas and low probabilities to homogeneous areas of the image. On the other hand it has to be taken into account that regions with a low sampling density are still sampled as the sampling density increases. This is important in order not to miss out fine details of the image which may occur in mostly homogeneous regions. We therefore define a probability mass function as the product of modified Gaussian functions centered at the already known sampling positions with a standard deviation of $\sigma[x, y]$. The modified Gaussian function,

$$p[x, y; m, n] = \left(1 - \exp\left(-\frac{(x-m)^2 + (y-n)^2}{\sigma[m, n]^2}\right)\right)^{\tau}, \tag{16}$$

for the central position $(m, n)$ comprises a zero at its center. In this way, the already sampled pixel at position $(m, n)$ cannot be drawn again. For pixels $(x, y)$ at larger distance, the probability soon reaches one. This is meaningful since the knowledge whether or not a region should be sampled is rather local. The value $\tau$ controls the steepness of the change from 0 to 1 of the modified Gaussian function. We use $\tau = 7$ as done in [12] resulting in a rather steep slope.

**Algorithm 1:** Pseudo Code for PADIS.

$b^0[x, y] \leftarrow$ initialize sampling pattern
$\tilde{f}^0[x, y] \leftarrow f[x, y] \cdot b^0[x, y]$ ▷Get first measurements
$i \leftarrow 0$
**while** $\sum_{x,y} b^i[x, y] < X \cdot Y$ **do**
  $v[x, y] \leftarrow$ (Eq. 8) ▷Calculate variance map
  $v_{\log} \leftarrow$ (Eq. 13) ▷Calculate logarithmic variance map
  $\sigma[x, y] \leftarrow$ (Eq. 14) ▷Calculate local standard deviation
  $P^i[x, y] \leftarrow$ (Eq. 17) ▷Calculate probability mass function
  $\delta_b^{i+1}[x, y] \leftarrow$ draw $N_+$ samples from $P[x, y]$
  $b^{i+1}[x, y] \leftarrow b^i[x, y] + \delta_b^{i+1}[x, y]$ ▷Update pattern
  $\tilde{f}^{i+1}[x, y] \leftarrow b^{i+1}[x, y] \cdot f[x, y]$ ▷Get measurements
  $\hat{f}^{i+1} \leftarrow$ reconstruction from $\tilde{f}^{i+1}[x, y]$ ▷For preview
  $i \leftarrow i + 1$
**end while**

Placing a modified Gaussian function at each already sampled position and taking the product yields the desired probability mass function $P^i[x, y]$,

$$P^i[x, y] = \prod_{(m,n)|b^i[m,n]=1} p[x, y; m, n], \tag{17}$$

which could be normalized such that $\sum_{x,y} P^i[x, y] = 1$ for convenience. Fig. 2(f) shows $P^i[x, y]$ for the exemplary image.

The derived probability mass function features similar characteristics as the variance map itself. Besides differences in the actual amplitudes and more clearly defined structures, it is important to note that the already sampled pixels are surrounded by a circular region where new samples are strongly suppressed as can be seen in Fig. 2(f). This ensures that neighboring pixels in heterogeneous areas are not sampled too densely. This is important in order not to waste measurements. Consequently enough samples are still spent on the homogeneous regions. At the same time, heterogeneous regions are still overall preferred compared to homogeneous regions.

During the $(i + 1)$-th step, the probability mass function $P^i[x, y]$ is used to draw new sampling positions $(x, y)$, which are stored in $\delta_b^{i+1}[x, y]$. In each iteration, a certain amount $N_+$ of new sampling positions is drawn before the probability mass function is recalculated. For convenience, PADIS is summarized in Algorithm 1.

## V. Simulations and Results

### A. Simulation Setup

Regarding the image datasets for our simulations, we use a set of scanning electron microscope images (SEM) [23] consisting of a wide range of biological samples, and the TECNICK image

Fig. 4. Four SEM images (left) and two TECNICK images (right) from the respective image datasets. The images are of size $1024 \times 576$ pixels and $1200 \times 1200$ pixels, respectively.

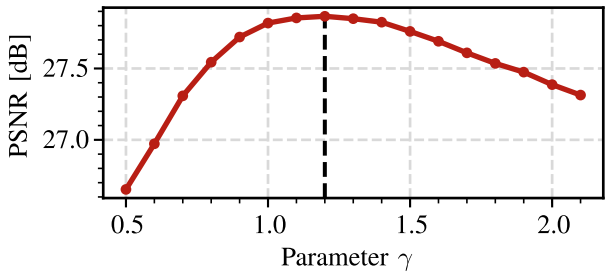


Fig. 5. Parameter training for the proportionality constant $\gamma$ of PADIS. The maximum is at $\gamma = 1.2$.

dataset [24] consisting of natural image content. For the SEM image dataset, only the 14 images available at a resolution of $1024 \times 768$ pixels are selected and the bottom 192 rows are cut away in order to remove the insets with the device setting. This resulted in images of size $1024 \times 576$ pixels. For the TECNICK images, all 100 images of size $1200 \times 1200$ pixels are used. Fig. 4 shows some of the images. The measurements are then simulated by a multiplication of the respective sampling patterns with the reference image as given in (1).

Subsequent to the measurement, the reconstruction of the full images is required. We use linear interpolation (LIN) as in [25], a custom weighted neighbor interpolation (WI) from the authors of SLADS [17], [18], steering kernel regression (SKR) [26], and frequency selective reconstruction (FSR) [10]. In order to judge the quality of the reconstructed images, the PSNR defined as

$$\mathrm{PSNR} = -10 \log_{10} \left( \frac{1}{X \cdot Y} \sum_{x,y} \left( f[x,y] - \hat{f}^i[x,y] \right)^2 \right) \tag{18}$$

with respect to the reference image $f[x,y] \in [0,1]$ is calculated and averaged for all images of a dataset at a fixed sampling density. In order to remove boundary effects, a border of 14 pixels is neglected in the PSNR calculation.

To generate the dynamic sampling patterns, the parameters of the algorithms need to be set. For the gradient based approach [16], we set the number of measurements added in each iteration to $N_+ = 1\%$ and initialize it with a random sampling pattern at a sampling density of $1\%$. Besides this, there are no further parameters to be adapted. For SLADS [17], [18], we performed a training of the regression function using the Kodak dataset [27]. The continuous variant of the implementation is chosen and the remaining default settings are left unchanged. As initialization, a random pattern at a sampling density of $1\%$ is chosen and 10 samples are added in each step. Half of the Kodak dataset [27] is used for the least square regression in the training. The other half is used to determine the optimal parameter $c$ of SLADS. Testing $c \in \{2, 4, 8, 16\}$, we find $c = 4$ being the best solution. SLADS uses a custom weighted neighbor interpolation (WI) for the required image reconstructions in this step. For SLADS-Net, we use the pre-trained model provided by the authors, which is trained on the cameraman image [19]. Again, the continuous variant of the implementation is chosen and the remaining default settings are left unchanged. In order to identify the parameter $c$, we created the dynamic sampling patterns for all images of the Kodak dataset using the provided models for $c \in \{2, 4, 8, 16\}$. We then compared the mean PSNR of the reconstruction results with LIN at a sampling density of $10\%$. This leads to $c = 2$ being the optimal parameter choice.

For PADIS the parameters were set as follows: We use $s_b = 6$ for the size of the weighting kernel of the weighted variance map which is small enough to keep the structures of the image visible but large enough to get a smooth result. For the number of samples added in each iteration, we set $N_+ = 1\%$ as for the gradient-based approach. Additionally, we perform a parameter optimization for the the parameter $\gamma$ required for the scaling of $\sigma_{\max}$ in (15). We use the Kodak dataset [27], a sampling density of $10\%$ and FSR [10]. Fig. 5 shows the PSNR result for different values of $\gamma$ leading to an optimal value of $\gamma = 1.2$, i.e., $\sigma_{\max} = 1.2/\sqrt{d_s}$. For the initialization of PADIS, we use the sampling pattern from [12] at a sampling density of $d_{\mathrm{init}} = 3\%$. This is high enough to ensure that the summations in (9) and (10) are not zero.

### B. Qualitative Comparison of the Different Sampling Patterns

Fig. 6 depicts the generated sampling patterns for the different static and dynamic sampling methods. For the dynamic sampling patterns, an exemplarily section of size $128 \times 128$ pixels from one SEM image is shown. For the static patterns, such a section is not representative. Therefore, the sampling patterns are shown for an auxiliary image of size $128 \times 128$ pixels. We observe that the gradient based approach, SLADS and SLADS-Net strongly focus on the edges. However, it is apparent that some details seem to be missed. For the proposed PADIS, the sampling pattern is also strongly adapting to the image content. However, it does not miss the details in the structure of the algae. Since the found details are sampled at a smaller density, the remaining sampling positions can be spend in other regions, which again allows to find further fine structures.

In order to actually judge the performance of the dynamic sampling approaches, it is required to take a look at the reconstruction results using appropriate reconstruction algorithms.

### C. Quantitative Evaluation of the Reconstruction Quality

Fig. 7 shows the reconstruction quality in terms of the average PSNR as a function of the sampling density. Here, the SEM dataset and FSR are used. The axes are clipped to the relevant sections. The lineskip sampling starts at very low reconstruction qualities and stays roughly -2dB below the other algorithms. It can serve as a baseline since this is a very simple approach.

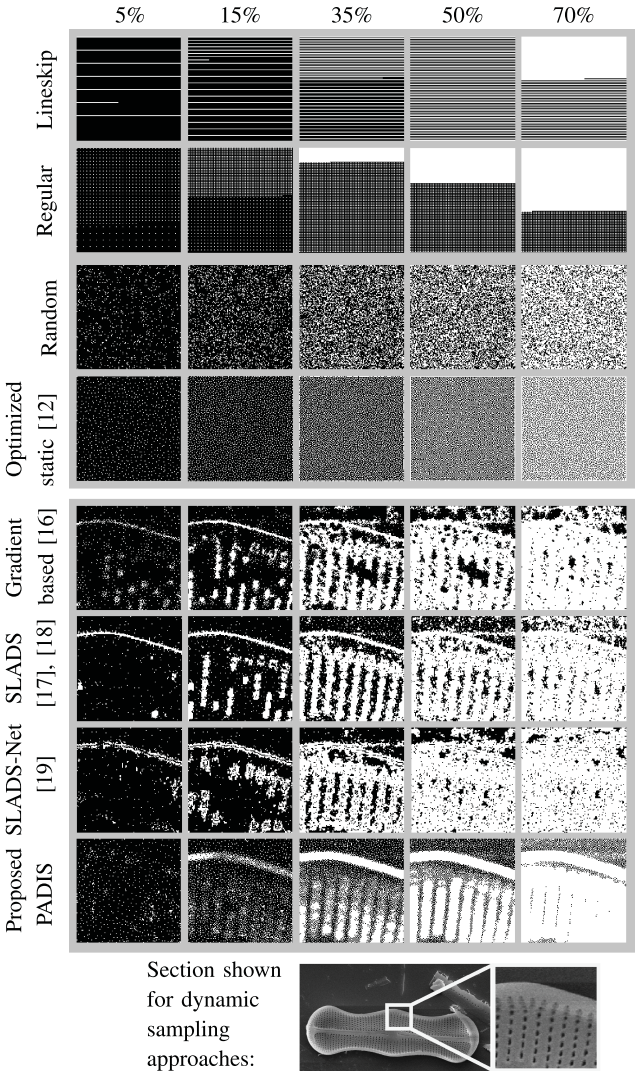


Fig. 6. Various static sampling patterns for an image of size 128 × 128 pixels (top) and sections of dynamic sampling patterns for an example from an SEM image (bottom). *(Please pay attention, additional aliasing may be caused by printing or scaling. Best to be viewed enlarged on a monitor.)*

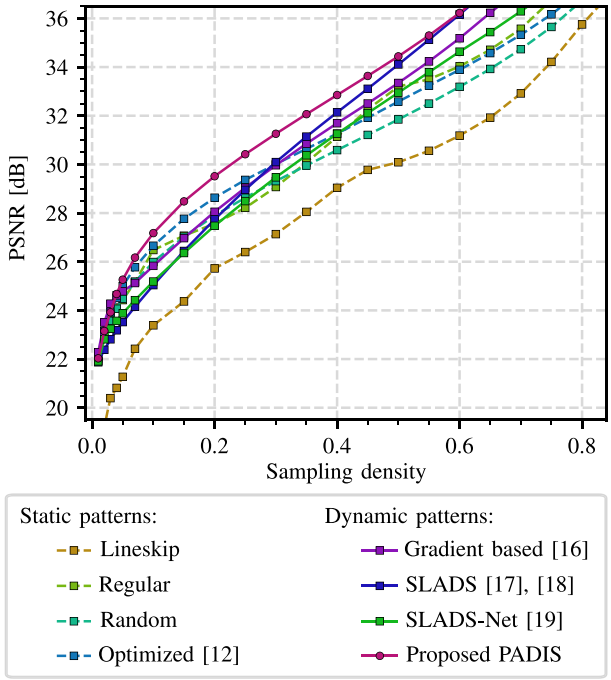


Fig. 7. Reconstruction quality in terms of average PSNR as a function of the sampling density for the SEM images and FSR as reconstruction method.

The regular pattern, the random pattern, and the optimized non-regular pattern from [12] achieve a reconstruction quality of more than 20dB even at a sampling density of 1%. Their reconstruction quality steadily increases for higher sampling densities and the optimized non-regular patterns from [12] perform better than the random and regular patterns as shown in the corresponding publication. Notably, the regular sampling pattern accomplishes a competitive reconstruction quality for sampling densities above 40%.

The proposed PADIS algorithm outperforms all static and dynamic patterns. Compared to the optimized non-regular sampling patterns from [12], it gains +0.72dB at a sampling density of 15% and +1.42dB at a sampling density of 35%. Comparing PADIS to the other dynamic approaches, gains of more than +1.51dB at a sampling density of 15% and +0.92dB at a sampling density of 35% are found. Interestingly, SLADS converges to the performance of PADIS at sampling densities larger than 60%.

In Table I we consider three additional reconstruction algorithms, namely LIN, WI, and SKR. Again, the SEM dataset is used and representative sampling densities are shown. For the gradient based approach [16] and SLADS [17], [18], we find that LIN results in a notably better reconstruction quality in terms of PSNR compared to FSR. Using each sampling method with its best reconstruction algorithm, PADIS surpasses the other dynamic sampling methods by more than +0.85dB at a sampling density of 15%, and +0.39dB at a sampling density of 35%. For 5% and 70%, PADIS with WI/FSR performs only -0.06dB and -0.3dB worse than the best choice from the other algorithms. Taking the overall performance across all sampling densities into account, we can summarize that PADIS is superior to the other sampling strategies in a majority of cases for the SEM dataset as can be seen from the values highlighted in bold font in Table I.

For the TECNICK dataset, a shortened overview of the results is given in Table II. We only show LIN and FSR and the most relevant sampling methods for convenience. Here, PADIS performs especially well for the sampling densities below 35% but is also very close to the optimal choices for the higher sampling densities. We would like to note again that even though the other dynamic sampling approaches have cases where they have slightly better reconstruction quality than PADIS, the proposed PADIS performs better taking all combinations of sampling densities, reconstruction algorithms and image datasets into account.

### D. Visual Comparisons

For a visual comparison of the reconstruction quality, Fig. 8 provides examples for three sampling densities. In terms of the

TABLE I
RECONSTRUCTION QUALITY IN TERMS OF AVERAGE PSNR IN DB USING THE SEM IMAGES FOR FOUR SAMPLING DENSITIES AND VARIOUS (DYNAMIC) SAMPLING PATTERNS. FOR THE RECONSTRUCTION, LINEAR INTERPOLATION (LIN), WEIGHTED INTERPOLATION (WI) FROM [17], STEERING KERNEL REGRESSION (SKR) [26], AND FREQUENCY SELECTIVE RECONSTRUCTION (FSR) [10] ARE USED. BOLD FONT HIGHLIGHTS THE BEST PSNR VALUE IN EACH COLUMN

| | 5% | | | | 15% | | | | 35% | | | | 70% | | | |
|---|---|---|---|---|---|---|---|---|---|---|---|---|---|---|---|---|
| SEM dataset (14 images) | LIN | WI | SKR | FSR | LIN | WI | SKR | FSR | LIN | WI | SKR | FSR | LIN | WI | SKR | FSR |
| Lineskip | 21.60 | 21.81 | 10.07 | 21.27 | 24.36 | 24.79 | 13.17 | 24.37 | 27.95 | 28.37 | 28.40 | 28.05 | 32.68 | 33.03 | 33.05 | 32.92 |
| Regular | 24.57 | 24.83 | 12.60 | 24.42 | 27.09 | 27.09 | 27.37 | 27.07 | 30.08 | 29.66 | 29.58 | 30.08 | 35.56 | 34.46 | 33.77 | 35.57 |
| Random | 24.37 | 24.58 | 18.68 | 24.48 | 26.68 | 26.68 | 26.92 | 27.03 | 29.31 | 29.22 | 29.39 | 29.95 | 33.71 | 33.72 | 33.17 | 34.73 |
| Optimized static [12] | 24.98 | 25.15 | **23.81** | 25.00 | 27.64 | 27.55 | 27.97 | 27.76 | 30.25 | 30.04 | 29.93 | 30.64 | 33.85 | 34.26 | 33.46 | 35.33 |
| Gradient based (dynamic) [16] | **25.39** | 24.95 | 15.04 | 24.78 | 27.63 | 27.07 | 17.05 | 26.97 | 31.42 | 30.84 | 21.33 | 30.85 | 37.64 | 37.33 | 30.54 | 37.24 |
| SLADS (dynamic) [17], [18] | 24.27 | 24.36 | 11.87 | 23.52 | 27.21 | 27.18 | 15.67 | 26.44 | 31.67 | 31.62 | 27.06 | 31.14 | **38.54** | **38.67** | **38.26** | **38.37** |
| SLADS-Net (dynamic) [19] | 24.18 | 24.27 | 12.70 | 23.88 | 26.50 | 26.48 | 15.69 | 26.36 | 30.25 | 30.30 | 20.37 | 30.38 | 35.57 | 35.83 | 28.85 | 36.29 |
| Proposed PADIS (dynamic) | 25.33 | **25.33** | 20.14 | **25.26** | **28.39** | **28.34** | **28.31** | **28.48** | **31.81** | **31.93** | **31.67** | **32.06** | 37.95 | 38.47 | 38.04 | **38.37** |

TABLE II
RECONSTRUCTION QUALITY IN TERMS OF AVERAGE PSNR IN DB USING THE TECNICK IMAGES FOR FOUR SAMPLING DENSITIES AND VARIOUS (DYNAMIC) SAMPLING PATTERNS. FOR THE RECONSTRUCTION, LINEAR INTERPOLATION (LIN), AND FREQUENCY SELECTIVE RECONSTRUCTION (FSR) [10] ARE USED. BOLD FONT HIGHLIGHTS THE BEST PSNR VALUE IN EACH COLUMN

| | 5% | | 15% | | 35% | | 70% | |
|---|---|---|---|---|---|---|---|---|
| TECNICK dataset (100 images) | LIN | FSR | LIN | FSR | LIN | FSR | LIN | FSR |
| Regular | 26.03 | 25.60 | 29.11 | 29.37 | 30.98 | 31.79 | 35.28 | 36.11 |
| Optimized static [12] | 26.06 | 26.73 | 30.03 | 31.41 | 33.78 | 35.71 | 37.73 | 40.66 |
| Gradient based (dynamic) [16] | **28.41** | 26.90 | 32.55 | 28.96 | 38.86 | 33.47 | 44.71 | 39.32 |
| SLADS (dynamic) [17], [18] | 25.89 | 23.46 | 31.76 | 28.68 | **39.68** | 37.82 | **49.40** | 48.66 |
| SLADS-Net (dynamic) [19] | 25.54 | 25.98 | 29.36 | 29.68 | 34.14 | 34.65 | 38.88 | 40.94 |
| Proposed PADIS (dynamic) | 27.45 | **28.06** | **32.69** | **33.92** | 38.24 | **39.44** | 48.66 | **49.05** |

reconstruction algorithm, LIN is chosen for the gradient based approach and SLADS, because this results in higher PSNR values than SKR and FSR as shown in Tables I and II. For the other methods, FSR is used for the reconstruction since it overall leads to better results. The PSNR of the individual image sections is provided as inset. It can be seen that PADIS significantly reduces the number of missing details and visual artifacts that occur for the other dynamic sampling approaches. The details of the algae in the SEM image are inconsistent for the gradient based approach, SLADS and SLADS-Net. Some of the structures are not yet recovered while others are sampled with high accuracy. This can straightforwardly be explained by taking the respective sampling patterns into account (see Figure. 6). The missing details are a direct consequence from the respective sampling patterns. As another example for visual artifacts, the roof of the house in the second image can be taken. It is incomplete for the gradient based approach, SLADS and SLADS-Net even at a sampling density of 35%. In both cases, PADIS leads to less visual artifacts and details can be recovered at lower sampling densities. Overall, the visual comparisons show that the gradient based approach, SLADS, and SLADS-Net miss out important details in presumably homogeneous regions, as they focus too much on the inhomogeneous parts of the image. For PADIS, this is not the case and more details of the image can be recovered while at the same time the sampling pattern is adapted to the content.

### *E. Noise Analysis*

In this section, we would like to elaborate on the effects arising in presence of measurement noise. Since all dynamic sampling algorithms depend on the measured data, measurement noise can impair the quality of the patterns and therefore the quality of the reconstruction. In order to get a first intuition about the role of measurement noise, we performed an experiment for the first SEM image of our dataset. We added Gaussian noise with a variance of $\sigma_{\mathrm{n}}^2 = 0.01$ to the image $f$. Afterwards, we run the (dynamic) sampling algorithms to acquire measurement data. For the reconstruction, LIN is used. We restrict the analysis to one simple reconstruction algorithm such that the influence of the reconstruction algorithm on noise is kept constant.

Fig. 9 shows the sampling patterns and reconstruction results for an exemplarily section at a sampling density of 15%. We observe that some of the dynamic sampling patterns are strongly altered in presence of noise. For the gradient based approach from [16], this can be explained by rather large gradients occurring from the measurement noise. For SLADS and SLADS-Net, similar observations are made. While SLADS finds different structures than before, SLADS-Net troubles to identify relevant parts and the altered sampling pattern has little resemblance to the noise-free sampling pattern. For PADIS, the sampling pattern is also altered though it still has a remarkable resemblance and the key features are still identified. This is due to the averaging used for calculating the variance in (8) as well as the fact that PADIS is based on a probability mass function. Consequently, even strong noisy alterations still give comparable sampling patterns. This is a key difference compared to the other maximization-based algorithms for which noisy measurement values can strongly influence the location of the maximum.

The reconstruction quality is mainly dominated by the noise present in the measurements. Nevertheless, for the given image sections, PADIS performs slightly better than the other methods in terms of PSNR. For the gradient based method, SLADS and SLADS-Net, disturbing artifacts arise in regions that are only sparsely sampled.

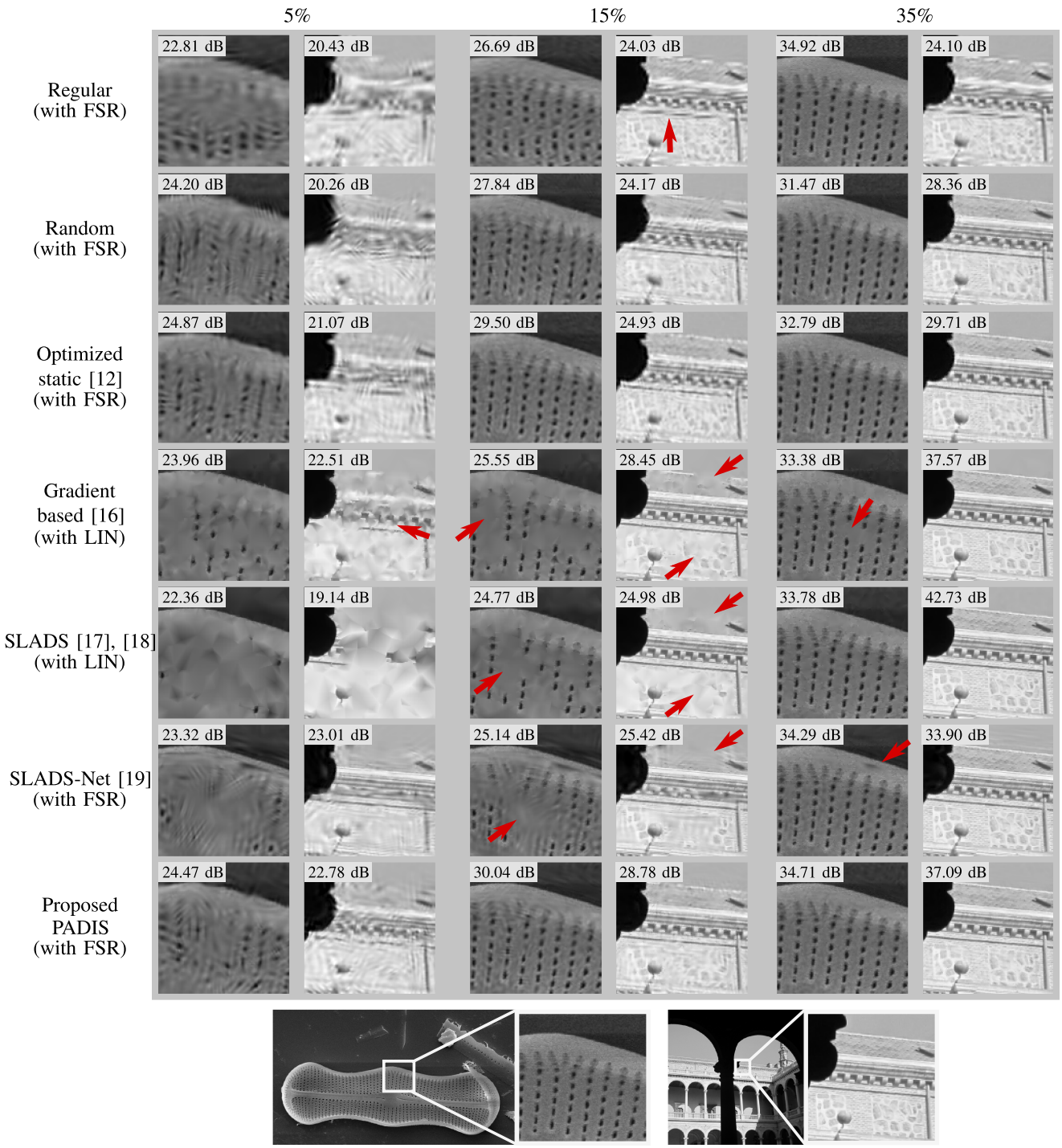


Fig. 8. Visual comparison of the reconstruction results using various static (first three rows) and dynamic (last four rows) sampling patterns. The reconstruction algorithm is chosen based on best average performance in Tables I and II. *(Please pay attention, additional aliasing may be caused by printing or scaling. Best to be viewed enlarged on a monitor.).*

### *F. Runtime Analysis*

In addition to the reconstruction quality, the runtime plays an important role in dynamic sampling. It is crucial since the dynamic patterns need to be calculated dynamically during the actual measurement process. All investigated dynamic sampling algorithms are written in Python allowing for a fair comparison. Table III summarizes the runtime to generate the sampling patterns up to a sampling density of 100%. One of the SEM images of size $1024 \times 576$ pixels is used. An Intel Xeon E3-2690 v2 processor with 3.0 GHz is used for the timings.

While the runtime for the gradient based approach [16] is in the same order of magnitude as PADIS, generating the patterns with SLADS [17], [18] and SLADS-Net [19] takes more than two orders of magnitude longer. PADIS is therefore a very good candidate for fast dynamic sampling. We would like to note

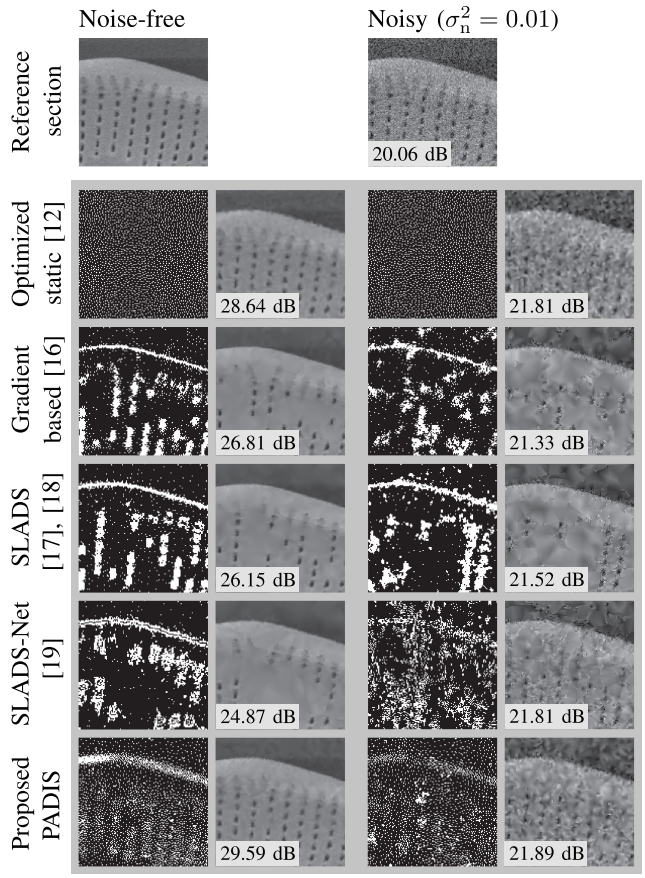


Fig. 9. The patterns and reconstruction results for the different dynamic sampling approaches are shown for the noise-free as well as the noisy scenario. For the reconstruction, LIN is used. The sampling density on the entire images is 15%. The PSNR with respect to the noise-free reference section is given as inset. *(Please pay attention, additional aliasing may be caused by printing or scaling. Best to be viewed enlarged on a monitor.)*.

TABLE III
RUNTIME (SMALLER IS BETTER) TO GENERATE THE DYNAMIC SAMPLING PATTERNS. THE RUNTIME RELATIVE TO THAT OF PADIS IS GIVEN, TOO. BOLD FONT HIGHLIGHTS THE BEST RESULT

| | Runtime in seconds | Relative runtime |
|---|---|---|
| Gradient based [16] | $2.0 \cdot 10^3$ s | 4.3 |
| SLADS [17], [18] | $1.2 \cdot 10^5$ s | 261 |
| SLADS-Net [19] | $1.0 \cdot 10^5$ s | 217 |
| Proposed PADIS | $\mathbf{4.6 \cdot 10^2}$ **s** | **1.0** |

that the runtimes for SLADS and SLADS-Net scale strongly non-linear with the sampling density and the size of the images. This is not an issue in the original publications [17], [18] and [19], since only tiny images were used. However, for mega-pixel images runtime increases tremendously for these two approaches. This non-linear scaling is not observed for the gradient based approach and the proposed PADIS, making those suitable also for very large images.

## VI. CONCLUSION

In this work, we proposed a novel probabilistic approach for dynamic sampling (PADIS). Our objective is to acquire a high quality image including texture and fine details as good as possible. Literature algorithms with similar objectives have shown to mainly perform well on images with clear shapes or segmented images [16]–[19]. PADIS aims at improving the state of the art for a broader class of image content including natural images. It incrementally adds new sampling positions by evaluating the local variance of previously sampled pixel values and creating a data driven probability mass function from which the next sampling positions are drawn. We compare PADIS with conventional static sampling approaches including a lineskip pattern, a regular pattern, a random pattern, and an optimized non-regular pattern, as well as three state of the art dynamic sampling algorithms from literature, namely the gradient based approach from [16], SLADS [17], [18] and SLADS-Net [19]. For the reconstruction of the images from the sampled data, we use different algorithms including frequency selective reconstruction (FSR) [10]. PADIS outperforms the static as well as the dynamic approaches for most combinations of image content, reconstruction algorithms, and sampling densities. Using a dataset of scanning electron microscope (SEM) images, a sampling density of 35% and FSR for reconstruction, gains of $+1.42$ dB compared to the best static sampling pattern and at least $+0.92$ dB compared to the other dynamic sampling methods are achieved. Even higher gains are found for natural image content.

Our findings are supported by visual examples showing that the image quality of the reconstructed images is superior using PADIS and reliable information about the image content can already be recovered using fewer samples. In presence of measurement noise, we showed that PADIS shows superior performance as its sampling patterns are less affected. Regarding the runtime of the algorithms, PADIS was 4.3-fold faster than the gradient based method. The other two methods required two orders of magnitude more processing time. Altogether, PADIS enables a high quality acquisition with less time and therefore potentially lower dose.

Future work will cover whether PADIS can be tailored specifically towards to the used reconstruction algorithm. In case of FSR, choosing appropriate sampling positions might help to distinguish between otherwise equally likely frequency components. A similar concept has been used for wavelet basis functions in [28]. Besides this, future image compression techniques based on PADIS are regarded to be promising. Other than in [20], the dynamically adapted sampling positions do not need to be transmitted as detailed in the introduction.

## REFERENCES

[1] H. S. Anderson, J. Ilic-Helms, B. Rohrer, J. Wheeler, and K. Larson, "Sparse imaging for fast electron microscopy," in *Proc. SPIE*, vol. 8657, Feb. 2013, Art. no. 86570C.

[2] S. B. Andersson and L. Y. Pao, "Non-raster sampling in atomic force microscopy: A compressed sensing approach," in *Proc. Amer. Control Conf.*, Jun. 2012, pp. 2485–2490.

[3] Y. Luo and S. B. Andersson, "A continuous sampling pattern design algorithm for atomic force microscopy images," *Ultramicroscopy*, vol. 196, pp. 167–179, Jan. 2019.

[4] S. Zhang *et al.*, "Dynamic sparse sampling for confocal Raman microscopy," *Analytical Chemistry*, vol. 90, no. 7, pp. 4461–4469, Mar. 2018.

[5] A. Béché, B. Goris, B. Freitag, and J. Verbeeck, "Development of a fast electromagnetic beam blanker for compressed sensing in scanning transmission electron microscopy," *Appl. Phys. Lett.*, vol. 108, no. 9, Feb. 2016, Art. no. 093103.

[6] L. Kovarik, A. Stevens, A. Liyu, and N. D. Browning, "Implementing an accurate and rapid sparse sampling approach for low-dose atomic resolution STEM imaging," *Appl. Phys. Lett.*, vol. 109, no. 16, Oct. 2016, Art. no. 164102.

[7] R. Egerton, P. Li, and M. Malac, "Radiation damage in the TEM and SEM," *Micron*, vol. 35, no. 6, pp. 399–409, Aug. 2004.

[8] M. A. Z. Dippé and E. H. Wold, "Antialiasing through stochastic sampling," in *Proc. 12th Annu. Conf. Comput. Graph. Interactive Techn.*, Jul. 1985, pp. 69–78.

[9] G. Hennenfent and F. J. Herrmann, "Irregular sampling: From aliasing to noise," in *Proc. 69th EAGE Conf. Exhib.*, Jun. 2007, Paper cp–27–00 063.

[10] J. Seiler, M. Jonscher, M. Schöberl, and A. Kaup, "Resampling images to a regular grid from a non-regular subset of pixel positions using frequency selective reconstruction," *IEEE Trans. Image Process.*, vol. 24, no. 11, pp. 4540–4555, Nov. 2015.

[11] S. Hwang, C. W. Han, S. V. Venkatakrishnan, C. A. Bouman, and V. Ortalan, "Towards the low-dose characterization of beam sensitive nanostructures via implementation of sparse image acquisition in scanning transmission electron microscopy," *Meas. Sci. Technol.*, vol. 28, no. 4, Feb. 2017, Art. no. 045402.

[12] S. Grosche, J. Seiler, and A. Kaup, "Design techniques for incremental non-regular image sampling patterns," in *Proc. IEEE Int. Conf. Imag. Syst. Techn.* , Oct. 2018, pp. 1–6.

[13] T. Dahmen *et al.*, "Feature adaptive sampling for scanning electron microscopy," *Scientific Rep.*, vol. 6, no. 1, pp. 1–11, May 2016.

[14] A. Taimori and F. Marvasti, "Adaptive sparse image sampling and recovery," *IEEE Trans. Comput. Imag.*, vol. 4, no. 3, pp. 311–325, Sep. 2018.

[15] T. Merryman and J. Kovacevic, "An adaptive multirate algorithm for acquisition of fluorescence microscopy data sets," *IEEE Trans. Image Process.*, vol. 14, no. 9, pp. 1246–1253, Sep. 2005.

[16] T. Dahmen and P. Trampert, "Sparse and adaptive sampling in scanning electron microscopy," *Microscopy Microanalysis*, vol. 25, no. S1, pp. 29–30, Feb. 2019.

[17] G. M. D. P. Godaliyadda, D. H. Ye, M. D. Uchic, M. A. Groeber, G. T. Buzzard, and C. Bouman, "A supervised learning approach for dynamic sampling," *Electron. Imag.*, vol. 2016, no. 19, pp. 1–8, Feb. 2016.

[18] G. M. D. P. Godaliyadda, D. H. Ye, M. D. Uchic, M. A. Groeber, G. T. Buzzard, and C. A. Bouman, "A framework for dynamic image sampling based on supervised learning," *IEEE Trans. Comput. Imag.*, vol. 4, no. 1, pp. 1–16, Mar. 2018.

[19] Y. Zhang, G. M. D. P. Godaliyadda, N. Ferrier, E. B. Gulsoy, C. A. Bouman, and C. Phatak, "SLADS-net: Supervised learning approach for dynamic sampling using deep neural networks," *Electron. Imag.*, vol. 2018, no. 15, pp. 131–1–1316, Jan. 2018.

[20] P. Peter, C. Schmaltz, N. Mach, M. Mainberger, and J. Weickert, "Beyond pure quality: Progressive modes, region of interest coding, and real time video decoding for PDE-based image compression," *J. Vis. Commun. Image Representation*, vol. 31, pp. 253–265, Aug. 2015.

[21] P. Peter, "Fast inpainting-based compression: Combining shepard interpolation with joint inpainting and prediction," in *Proc. IEEE Int. Conf. Image Process.* , Sep. 2019, pp. 3557–3561.

[22] G. M. D. P. Godaliyadda, G. T. Buzzard, and C. A. Bouman, "A model-based framework for fast dynamic image sampling," in *Proc. IEEE Int. Conf. Acoust., Speech Signal Process.*, May 2014, pp. 1822–1826.

[23] Museo delle Scienze, "SEM images from MUSE - Science museum," Apr. 2016. [Online]. Available: https://commons.wikimedia.org/wiki/Category:SEM_images_from_MUSE_-_Science_Museum, Accessed: May 18, 2018.

[24] N. Asuni and A. Giachetti, "Testimages: A large-scale archive for testing visual devices and basic image processing algorithms," in *Proc. Smart Tools Apps Graph. - Eurograph. Italian Chapter Conf.*, Sep. 2014, pp. 63–70.

[25] E. Jones *et al.*, "SciPy: Open source scientific tools for Python," 2001. [Online]. Available: http://www.scipy.org/

[26] H. Takeda, S. Farsiu, and P. Milanfar, "Kernel regression for image processing and reconstruction," *IEEE Trans. Image Process.*, vol. 16, no. 2, pp. 349–366, Feb. 2007.

[27] "Kodak test images," Jan. 2013. [Online]. Available: http://r0k.us/graphics/kodak/

[28] Z. Devir and M. Lindenbaum, "Blind adaptive sampling of images," *IEEE Trans. Image Process.*, vol. 21, no. 4, pp. 1478–1487, Apr. 2012.


**Simon Grosche** received the master's degree in physics from Friedrich-Alexander University Erlangen-Nürnberg (FAU), Germany, in 2017. During his studies, he was a Fellow of German Academic Scholarship Foundation. During his masters, he worked on polarization tailored light fields and nano-optics and conducted his thesis at the Max Planck Institute for the Science of Light, Erlangen and the University of Ottawa, Canada.

Since 2017, he has been a Researcher with the Chair of Multimedia Communications and Signal Processing at Friedrich-Alexander University Erlangen-Nürnberg (FAU), Germany, where he conducts research on sparse sampling and reconstruction techniques in image and video signal processing.

**Michael Koller** received the master's degree in electrical engineering from Friedrich-Alexander University Erlangen-Nürnberg (FAU), Germany, in 2019. During his master's at the Chair of Multimedia Communications and Signal Processing, FAU, he worked on sparse image sampling and reconstruction techniques and its application to image compression. Since 2019, he has been with MBDA Germany as a Development Engineer for image processing algorithms. His research interests include image processing, computer vision and machine learning.

**Jürgen Seiler** (Senior Member, IEEE) received the habilitation degree in 2018, the doctoral degree in 2011, and the diploma degree in electrical engineering, electronics and information technology in 2006. He is a Senior Scientist and Lecturer with the Chair of Multimedia Communications and Signal Processing at the Friedrich-Alexander Universität Erlangen-Nürnberg, Germany. he has authored or coauthored more than 90 technical publications.

His research interests include image and video signal processing, signal reconstruction and coding, signal transforms, and linear systems theory.

He received the dissertation award of the Information Technology Society of the German Electrical Engineering Association as well as the dissertation award of the Staedtler-Foundation, both in 2012. In 2007, he received diploma awards from the Institute of Electrical Engineering, Electronics and Information Technology, Erlangen, as well as from the German Electrical Engineering Association. He also received scholarships from the German National Academic Foundation and the Lucent Technologies Foundation. He is the co-recipient of four Best Paper Awards.

**André Kaup** (Fellow Member, IEEE) received the Dipl.-Ing. and Dr.-Ing. degrees in electrical engineering from RWTH Aachen University, Aachen, Germany, in 1989 and 1995, respectively.

He joined Siemens Corporate Technology, Munich, Germany, in 1995 and became Head of the Mobile Applications and Services Group in 1999. Since 2001, he has been a Full Professor and the Head of the Chair of Multimedia Communications and Signal Processing at Friedrich-Alexander University Erlangen-Nürnberg (FAU), Germany. From 1997 to 2001, he was the Head of the German MPEG delegation. From 2005 to 2007, he was a Vice Speaker of the DFG Collaborative Research Center 603. From 2015 to 2017, he was the Head of the Department of Electrical Engineering and Vice Dean of the Faculty of Engineering at FAU.

André Kaup is a member of the IEEE Multimedia Signal Processing Technical Committee, a member of the scientific advisory board of the German VDE/ITG, and a Fellow of the IEEE. He was an Associate Editor for IEEE TRANSACTIONS ON CIRCUITS AND SYSTEMS FOR VIDEO TECHNOLOGY and was a Guest Editor for IEEE JOURNAL OF SELECTED TOPICS IN SIGNAL PROCESSING. He was a Siemens Inventor of the Year 1998 and obtained the 1999 ITG Award. He was recipient of the several Best Paper Awards including the Paul Dan Cristea Special Award in 2013, and his group won the Grand Video Compression Challenge at the Picture Coding Symposium 2013. The Faculty of Engineering at FAU honored him with the Teaching Award in 2015. In 2018, he was elected full member of the Bavarian Academy of Sciences.

He has authored around 350 journal and conference papers and has over 120 patents granted or pending. His research interests include image and video signal processing and coding, and multimedia communication.